Two-color nanoscopy of three-dimensional volumes by 4Pi detection of stochastically switched fluorophores

Daniel Aquino[1], Andreas Schönle[1], Claudia Geisler[1,3], Claas v Middendorff[1], Christian A Wurm[1], Yosuke Okamura[2], Thorsten Lang[2], Stefan W Hell[1] & Alexander Egner[1,3]

We demonstrate three-dimensional (3D) super-resolution imaging of stochastically switched fluorophores distributed across whole cells. By evaluating the higher moments of the diffraction spot provided by a 4Pi detection scheme, single markers can be simultaneously localized with <10 nm precision in three dimensions in a layer of 650 nm thickness at an arbitrarily selected depth in the sample. By splitting the fluorescence light into orthogonal polarization states, our 4Pi setup also facilitates the 3D nanoscopy of multiple fluorophores. Offering a combination of multicolor recording, nanoscale resolution and extended axial depth, our method substantially advances the noninvasive 3D imaging of cells and of other transparent materials.

For many decades, the noninvasive fluorescence imaging of cells at the suborganelle level has been limited by diffraction to a resolution of about half the wavelength of light ($\lambda/2$) in the focal plane (x, y) and to about λ along the optic axis (z). The disparity between the x–y- and the z-dimension resolution stems from the fact that a lens focuses and detects just a segment of a complete spherical wavefront. By coherently adding the spherical wavefront segments of two opposing high-angle lenses for illumination and/or fluorescence detection, the microscope aperture can be extended along the z axis, increasing the z-dimension resolution by three- to sevenfold[1–4]. The gain in axial resolution directly translates into increased precision when determining the position of nanosized fluorescent objects or molecules[5,6]. Introduced in imaging through the concept of 4Pi microscopy[1,3,4], the interference of an emitted photon with itself at the detector after having passed through opposing lenses is also essential in I^{5}M microscopy[2]. This photon self-interference is described by two spherical wavefronts of fluorescence light propagating in opposite directions and interfering at the detector plane. Notably, unambiguous axial superresolution with opposing lenses requires high-angle spherical wavefront segments. Using just interfering plane waves limits this strategy to objects thinner than $\lambda/2$ (~250 nm) because of periodic replication artifacts[4].

The 4Pi and I^{5}M schemes push three-dimensional (3D) imaging to the diffraction limit, but overcoming this limit requires a molecular transition to make fluorophores distinct within subdiffraction distances[7] such as a transition between a fluorescent and a dark state. Whereas stimulated emission depletion (STED) microscopy[8,9] and related methods predefine the spatial coordinates at which fluorophores are allowed to assume the fluorescent state, in stochastic super-resolution modalities[10–13] the fluorophores are allowed to assume the fluorescent state stochastically at an unknown position in space so that only one fluorophore is likely to emit in a region covered by diffraction. Depending on the specific molecular transition used, the stochastic mode is known as photoactivated localization microscopy (PALM)[10], stochastic optical reconstruction microscopy (STORM)[11,14], fluorescence PALM (FPALM)[12], PALM with independently running acquisition (PALMIRA)[13,15], ground state depletion microscopy (GSDIM)[16], direct STORM (dSTORM)[15,17] or others; here we refer to it as the stochastic mode or single marker switching (SMS) microscopy.

By taking advantage of an enlarged aperture angle, 4Pi systems clearly outperform their single-lens counterparts in both the coordinate-predefined and the stochastic mode[18,19]. IsoSTED microscopy[19,20] has thus yielded a resolution of < 21 nm and 30 nm in the lateral and axial directions, respectively. In the stochastic mode, 4Pi fluorescence detection records twice the number of photons, thus increasing the localization precision by about $\sqrt{2}$ in all directions and by an additional about fourfold along the z axis[18]. The first realization of this scheme, called interferometric PALM (iPALM)[21], has thus achieved an impressive resolving power, with localization precisions of ~9.8 nm (z) and 22.8 nm (x, y) in full-width half-maxima (FWHM).

However, the iPALM studies were challenged by z-dimension localization ambiguities for layers thicker than $\lambda/2$ (225 nm), limiting iPALM to ultraflat structures or to the proximity of the coverslip. This limitation stems from the fact that in iPALM the emitted wavefronts are analyzed as plane waves. Much like the z-dimension ambiguity problem had been solved via 4Pi

[1]Max Planck Institute for Biophysical Chemistry, Department of NanoBiophotonics, Göttingen, Germany. [2]Membrane Biochemistry Laboratory, Life and Medical Sciences Institute, University of Bonn, Bonn, Germany. [3]Present address: Laser Laboratory Göttingen e.V., Department of Optical Nanoscopy, Göttingen, Germany. Correspondence should be addressed to S.W.H. (shell@gwdg.de) or A.E. (aegner@gwdg.de).

RECEIVED 15 JULY 2010; ACCEPTED 14 FEBRUARY 2011; PUBLISHED ONLINE 13 MARCH 2011; DOI:10.1038/NMETH.1583

microscopy by resorting to spherical rather than plane waves, we now solved this problem in the stochastic superresolution modalities by considering the spherical shape of the wavefronts describing the simultaneous passage of the emitted photons through both objective lenses. Thus we constructed a 4Pi-SMS microscope (that is, 4Pi-PALM, 4Pi-STORM, 4Pi-GSDIM and so on) with a demonstrated resolution potential of at least 5.4–6.6 nm in the axial and 8.3–22.3 nm in the lateral direction (FWHM) within an about 1.5λ-thick (~650 nm) optical layer around the focal plane, placed to any z-dimension position in the sample. The thickness of the layer can be extended to 2λ with the resolution slightly decreasing at the edge. The sample can be thicker than 1 μm because emitters outside this layer can be identified and excluded. Our 4Pi-SMS setup elegantly accommodated multiple labels. We demonstrated to our knowledge the currently unique combination of resolution, depth of field and multicolor detection by imaging the 3D distribution of proteins in cells.

RESULTS

Experimental setup and theory

The 4Pi-SMS setup (**Fig. 1a**) features a triangular 4Pi cavity[3] with an additional achromatic quarter-wave plate and a modified Babinet-Soleil compensator (**Supplementary Fig. 1**) in each leg of the triangle. The optical axes of the quarter-wave plates and the setup plane draw an angle of 45°, ensuring that the fluorescence ends up with nearly equal probability in the s- and p-polarized channels irrespective of the fluorophore orientation. The Babinet-Soleil compensators retard the phase of the p-component of the fluorescence with respect to its s-polarized component within both leg a and leg b by $\Delta\varphi_a$ and $\Delta\varphi_b$, respectively, thus creating time-separated fluorescence wave packages with mutually orthogonal polarization. After interference at the neutral beam splitter, the ensuing optical elements separate the packages in four detection channels (s1, s2, p1 and p2), and project each one onto a single electron-multiplying charge-coupled device (EMCCD) camera in a 2 × 2 grid pattern. In this scheme, each fluorescence photon can pass through both lenses simultaneously, can self-interfere at the beam splitter and thus be detected with certain probabilities in any of the four channels. Conceptually relevant phenomena take place up to the beam splitter; components after the beam splitter merely facilitate the use of a single camera.

The lateral position (x_0, y_0) of emission can be determined in each channel by localization. Here we used Hogbom's classical CLEAN algorithm in conjunction with a mask-fitting algorithm of the respective Airy spot[13]. We calculated the final lateral position as the intensity-weighted average of the positions determined in each channel and projected them into a common coordinate system using an affine transformation determined from calibration measurements (**Supplementary Note 1**). For z-position determination, we adjusted the 4Pi cavity such that (i) the electric field from an emitter located in the common focal plane ($z = 0$) features the same phase difference at the beam splitter, irrespective of the emission wavelength and the lateral position of the marker and (ii) $\Delta\varphi_a - \Delta\varphi_b = \pi/2$.

We plotted the theoretical (Gaussian-weighted) fluorescence as a function of the z position of a point source for each of the four detection channels (**Fig. 1b**). The four signals oscillate as the point source is moved along the z direction; note that the relative phases of the individual channels are evenly spaced within the 0–2π interval. Relative intensities of the four channels yield a global phase φ_0, which specifies the average phase difference of the electric field of the fluorescence at the beam splitter. φ_0 ranges from $-\pi$ to π and can be used to determine the z position within an axial interval $\Delta z_0 \cong \lambda/2$, for example, 250 nm (**Supplementary Note 1**). However, the fluorophores located outside this $\lambda/2$ thick sheet will be incorrectly projected into this sheet, leaving imaging artifacts (**Supplementary Fig. 2**).

We solved this problem by exploiting the fact that the phase difference between the counterpropagating wavefronts leaving the lenses varies more slowly at the outer parts when the emitter moves out of focus (**Fig. 1**). To this end, we calculated the global phase not only for the Gaussian-weighted intensity of the fluorescence spot on the camera but also for its Gaussian-weighted third central moment (**Fig. 1c**), which has a larger contribution from the inner wavefront parts. The resulting phase pair (φ_0, φ_3) uniquely encodes the z position of the marker over a range >$\lambda/2$ (**Supplementary Figs. 3** and **4** and **Supplementary Note 1**). The focal plane ($z = 0$) is identified by $\varphi_0 = \varphi_3$ (**Fig. 1d**).

Characterization of the 4Pi-SMS setup

To explore our measurement principle, we scanned a 100-nm-diameter bead from $z = -500$ nm to $z = 500$ nm in 40-nm steps, recording 300 frames at each position, with on average ~2,700 photons per frame. We unambiguously determined the bead's z position over this entire z range (**Fig. 1e**). Fitting a Gaussian to the histograms of the z localizations for two selected positions, we determined the axial localization precision to be 2.6 nm and 2.8 nm for $z = -181$ nm and 180 nm, respectively. By fitting a Gaussian to the main peak of the position histogram for each location, we estimated the overall axial and lateral localization precision as σ_z = ~2.3–3.5 nm and σ_{xy} = ~3.5–17.5 nm, respectively (**Fig. 1f**,**g**). Whereas the precision degrades toward the edge of the axial range, it was already in the order of the residual setup instability in the most central part. Note that the bead is a nearly isotropic emitter because it contains many randomly oriented fluorophores. The localization of single emitters will be limited by the typically lower photon budget and, in the case of largely static molecules, by systematic errors owing to emission anisotropies occurring when the emission dipole is tilted with respect to the z axis and the focal plane[22]. For practical biological imaging, other limiting factors, such as the linker length between the target epitope and the marker or the labeling density, can reduce the effective resolution below the localization precision.

Toward the edge of the axial imaging range, we observed a slightly increased probability of incorrect assignment of the bead position to planes located at a distance Δz_0 above and below the actual plane. This was due to the lateral spreading of the diffraction spot for emitters farther away from the focal plane and the concomitant increase of noise (**Supplementary Fig. 4**). This probability was on average below 2% over the entire z range, and typically 0.75% for the most central 650 nm. To evaluate the role of instabilities, we imaged a bead located at $z = 0$ at different excitation intensities (**Supplementary Fig. 5**). By discriminating the error from the count rate–dependent localization precision, we found a coordinate instability of ~2 nm.

Imaging fibrinogen receptors on activated platelets

To explore the capacity of 4Pi-SMS microscopy for unambiguous imaging in samples thicker than $\lambda/2$, we first imaged the

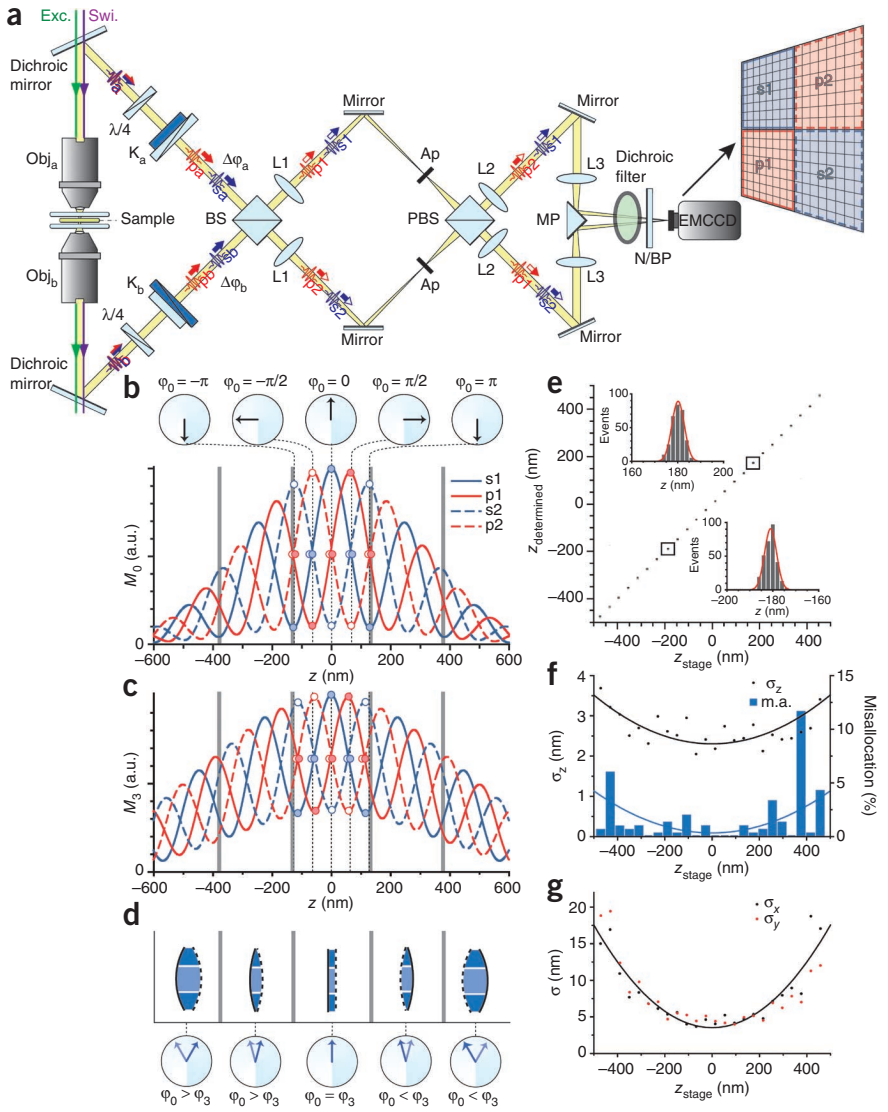

Figure 1 | The 4Pi-SMS microscope. (**a**) The sample is sandwiched between two coverslips. Illumination for excitation (exc.) and on-off switching (swi.) occurs through the upper of the two water immersion objective lenses (Obj_a and Obj_b). The 4Pi cavity consists of two dichroic mirrors, two quarter-wave plates ($\lambda/4$), two modified Babinet-Soleil compensators (K_a and K_b) and a neutral beam splitter (BS). The linear s- and p-polarization states (sa, pa, sb and pb) are separated by the compensators in each cavity arm, and a respective phase difference ($\Delta\varphi_a$, $\Delta\varphi_b$) is introduced. The superimposed intermediate image pairs p1 and s1, and p2 and s2, generated by the tube lenses (L1), are clipped by the variable apertures (Ap) to fill one quadrant each of the EMCCD chip in parallel. The polarizing beam splitter (PBS) interchanges the partners of the image pairs, which are then imaged via lenses L2 and L3, the metalized prism (MP), a notch filter rejecting the excitation light, and a bandpass filter (N/BP) onto the camera. The mirrors are tilted to spatially separate the four detection channels. For two-color imaging, a dichroic filter can be placed in front of the camera. (**b**,**c**) Gaussian-weighted signal (M_0; **b**) and Gaussian-weighted third central moment (M_3; **c**) of the detection channels plotted as a function of the axial marker position. (**d**) The propagation of fluorescence light from out of focal plane emitters is described by a segment of a spherical wavefront. Solid and dashed lines represent the wavefronts corresponding to Obj_a and Obj_b, respectively. Phase difference between wavefronts is indicated in dark and light blue for the outer and inner parts of the counterpropagating wavefronts, respectively. (**e**) Plot of located versus stage position. For each stage position, 300 independent localizations were performed. Insets show distributions of *z* localizations for the boxed *z* positions. (**f**) Axial localization precision (σ_z) for a fluorescent bead containing randomly oriented emitters and the amount of mislocalization. (**g**) Lateral localization precision for *x* dimension (σ_x) and *y* dimension (σ_y). Solid curves in **f** and **g** represent cubic polynomial fits to the data.

distribution of fibrinogen receptors on human platelets, placed onto coverslips carrying a thrombin-coated nanosheet[23], which form clusters upon platelet activation[24]. We visualized the glycoprotein IIb/IIIa (GPIIb/IIIa) receptor complex by staining GPIIb using the photochromic Rhodamine S and the fluorescent dye Atto 532. Unlike in iPALM experiments[21], we did not confine the light field to a layer thinner than Δz_0 (~250 nm). Platelets are smooth, disc-shaped cells of ~3 µm diameter and are typically 1 µm thick. Upon surface activation, they adhere and spread over a stellate shape into a 'fried egg' form[25].

We plotted an *x*-*y* 'histogram image' of the molecular positions recorded from a partially activated platelet labeled with Rhodamine S (**Fig. 2a**). We acquired 30,000 images at a 100 Hz frame rate with continuous wave excitation of 7–14 kW cm^{-2} intensity at 532 nm. Irradiation with activating UV light was not required because at pH 7 the Rhodamine S molecules switch thermally back to their fluorescent 'on' state sufficiently quickly. The estimated localization precision was σ_z = ~5 nm and σ_{xy} = ~10 nm. We clearly observed the stellate cell shape. The protuberances had a round profile and tapered to their end (**Fig. 2b**,**c**). The *z*-position histograms confirmed this finding (**Fig. 2d**,**e**).

We plotted an *x*–*y*-position histogram image of a platelet in which GPIIb was stained with Atto 532 (120,000 images recorded at 7–14 kW cm^{-2}, 532 nm), exhibiting the 'fried egg' shape (**Fig. 2f**). The estimated localization precision was σ_z = ~7 nm and σ_{xy} = ~14 nm. In the images, the cell could be recognized as a whole, with the upper membrane forming an arch on top of the lower membrane at the periphery. The membranes converged before diverging again, with the upper membrane reaching out to form a cupola. We identified individual receptor clusters on the activated platelet plasma membrane. To visualize the membrane 'run', we plotted a *y*–*z*-position histogram image of all fluorophore positions in a central cross-section of the cell and could resolve the two membranes over the entire section (**Fig. 2g**). Owing to the <10% probability of assigning an event to the wrong period, we observed a faint ghost image above the cell, which has no influence on the localization precision of the correctly assigned events (>90%). We plotted histograms of the *z* position for selected regions marked in

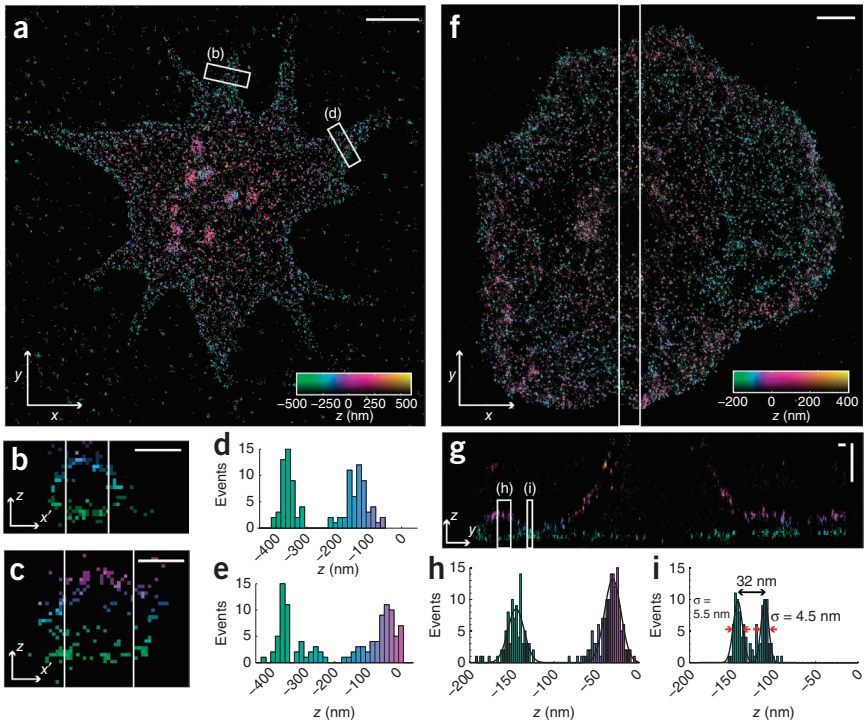

Figure 2 | 4Pi-SMS imaging of human platelets. (**a**) An *x*–*y* histogram image of the Rhodamine S–labeled GPIIb/IIIa receptor of a partially activated platelet. The color encodes the axial position of each label. (**b**,**c**) *x*′–*z* image (3D position data contracted in *y*′ direction) of the distribution of labels located in the respective regions indicated in **a**. The color encodes *z* values as in **a**. (**d**,**e**) *z*-position histograms for the regions marked in **b** and **c**, respectively. (**f**) *x*–*y* histogram image of the Atto 532–labeled GPIIb/IIIa receptor of a fully activated platelet. (**g**) *y*–*z* histogram image (that is, 3D position data contracted in *x* direction) of the distribution of labels located in the region marked in **f**. The *z* axis is stretched by a factor of five. (**h**,**i**) *z*-position histograms for the regions marked in **g**. Red arrows indicate FWHM. Scale bars, 1 µm (**a**,**f**), 200 nm (**b**,**d**), 200 nm (**g**) in *x* direction and *z* direction.

Figure 2g (**Fig. 2h**,**i**). The height of the arch at the left position marked in **Figure 2g** was ~115 nm (**Fig. 2h**) and the distributions of estimated fluorophore positions had a σ of ~4.5 nm and ~5.5 nm where the upper and the lower membrane images were narrowest (**Fig. 2i**), corresponding to FWHMs of 10.6 nm and 13.0 nm; the FWHM gives a conservative estimate of the practical resolution. The obtained precision enabled us to discriminate the upper from the lower membrane fluorophores even at their closest distance of 32 nm. Likewise, toward the center of the cell where the membranes are farther apart than $\Delta z_0 = 255$ nm, the run of the upper membrane was reproduced with equal confidence. The wider distributions in **Figure 2h** can be attributed to the membrane curvature and a wider dye distribution; therefore the upper membrane appeared fainter for large *z* positions.

Imaging of microtubules inside cultured mammalian cells

As platelets are comparatively thin, we also imaged the microtubule cytoskeleton inside Vero cells in which α-tubulin was stained with Rhodamine S. We adjusted the focal plane roughly to the cell middle and recorded 110,000 frames at 100 frames per second, with continuous wave excitation at 532 nm and with 7–14 kW cm^{-2} intensity. Activating UV light was not required. We plotted an *x*–*y* histogram image of the molecular positions for $z = \pm 500$ nm (**Fig. 3a**). The localization precision was $\sigma_z = \sim 6$ nm and $\sigma_{xy} = \sim 10$ nm.

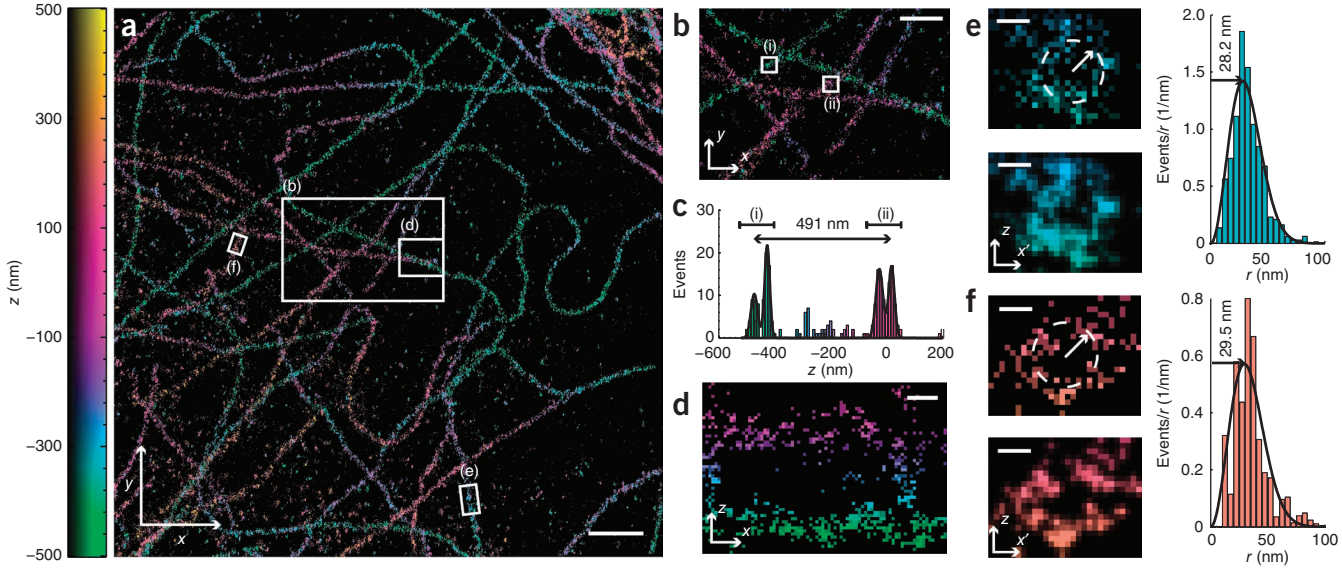

Figure 3 | 4Pi-SMS imaging with extended axial depth. (**a**) *x*–*y* histogram image of Rhodamine S–labeled tubulin in a Vero cell. The color encodes the axial position of each label. (**b**) Close-up of the area indicated in **a**. (**c**) *z*-position histograms for the two regions marked in **b**. (**d**) *x*–*z* histogram image of the area indicated in **a**. (**e**,**f**) *x*′–*z* histogram image of the distribution of labels located in respective areas indicated in **a** (top), the same images smoothed with a Gaussian (σ = 3.2 nm) for better visibility and respective radial-position histograms. $r = (x'^2 + z^2)^{0.5}$. Scale bars, 1 µm (**a**), 500 nm (**b**), 100 nm (**d**), 30 nm (**e**,**f**).

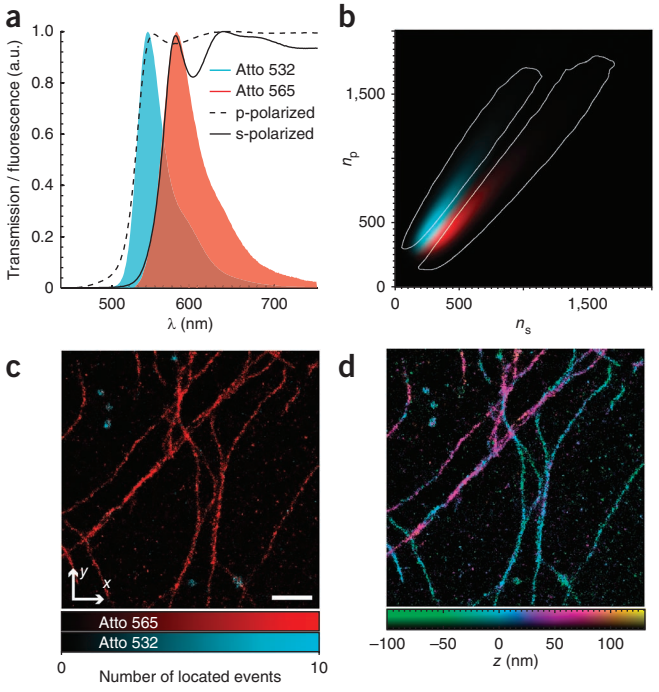

Figure 4 | Two-color imaging. (**a**) Fluorescence emission spectra of Atto 523 and Atto 565 as well as the transmission spectrum for s- and p-polarized light of the long-pass filter. (**b**) s-p histogram of events in the gauge measurement performed on samples immunostained for peroxysomes (Atto 532, cyan) and microtubles (Atto 565, red). Events from Atto 532 had a larger ratio of photons in the p channel versus the s channel (n_p and n_s) owing to the higher transmission of the dichroic. White contours enclose areas with a classification confidence better than 80%. Only events inside these regions were used subsequently, reducing the cross-talk to < 6%. (**c**) *x*–*y* histogram image of a PtK2 cell immunostained for both peroxysomes (Atto 532) and microtubles (Atto 565). Scale bar, 1 µm. (**d**) *x*–*y* histogram image of the same cell as in **c** color-coded for *z* position.

We observed the filamentous network distributed over a *z*-value range of ~491 nm (**Fig. 3b**,**c**). The *z*-position histogram of the markers associated with the lower fiber had two distinct peaks with a σ of 12.2 nm and 9.2 nm separated by 46.2 nm; the markers associated with the upper fiber had two distinct peaks with a σ of 12.9 nm and 10.6 nm separated by ~43.5 nm. As this is in good agreement with the diameter of microtubules (~25 nm) plus double the distance of the label from the epitope recognized by the primary antibody (~10 nm), the 4Pi-SMS setup most likely discerns the upper from the lower part of the microtubule. In another region of the cell (**Fig. 3d**), two fibers with a *z* separation of 297–374 nm were clearly discerned, and at some coordinates, the labels associated with the upper and lower part of the microtubule were apparent. To test whether our setup can indeed resolve how the fluorophores reside around the microtubules, we extracted *x*-*z* position histogram images integrated a few tens of nanometers along the microtubules (**Fig. 3e**,**f**; see **Supplementary Fig. 6** for more examples). To accentuate the ring-like shape of the fluorophore distribution we also plotted a slightly smoothed version of the histogram images. This smoothing has a similar effect as drawing a Gaussian at each fluorophore coordinate, a representation frequently used for PALM data. From the respective radial-position histograms, we determined the ring diameter to be ~60 nm.

Two-color imaging

Our concept of solving the *z*-dimension ambiguity problem by exploiting the spherical shape of the fluorescence wavefronts is more generally applicable, particularly to iPALM, that is, to a system with three detection channels separated by phase shifts of 2π/3. The full potential of our four-channel scheme comes into effect when imaging multiple colors. Multicolor imaging can be easily realized without additional detection channels, which is less straightforward with a three-channel system. Because the ratio of the combined s-polarized versus the p-polarized emission components just depends on the type of emitter but not on its position, we can classify multiple fluorophore species by such a ratio[26]. More generally, the 4Pi-SMS setup is tuned to translate an unmistakable hallmark of the fluorescence emission of a label species into a characteristic value of this ratio, so that the species is automatically divulged.

For example, we achieved two-color imaging by placing an additional long-pass filter in front of the camera (**Fig. 1a**). We plotted the emission spectra of Atto 532 and Atto 565 as well as the transmission characteristics of our long-pass filter under 45° illumination (**Fig. 4a**). The edge of the filter for the s-polarized light is shifted by ~30 nm from that for the p-polarized light, such that placing it in the detection path changes the relative detection efficiency of the s-polarized versus p-polarized fluorescence for Atto 532 and Atto 565 to 0.50 and 0.81, respectively. The 2D histogram in s–p space created from our gauge measurement with single-labeled samples (**Fig. 4b**) shows that this method enables the classification of individual Atto 532 and Atto 565 molecules based on the ratio between the two channels. This is exemplified in an *x*–*y* histogram image of the molecular positions derived from a PtK2 cell immunostained for peroxysomes (Atto 532 label) and microtubules (Atto 565 label) (**Fig. 4c**). The dichroic mirror does not split the images but just attenuates the polarizations unevenly. Hence, the two channels are inherently aligned. Errors in the lateral position owing to transverse chromatic aberrations should be negligible because the detected spectra are strongly overlapping. Chromatic effects on the z-localization are excluded by our calibration procedure (**Supplementary Note 1**). Molecules that cannot be classified are discarded, which trades off dynamic range for lower cross-talk[26]. We included events for which the gauge measurement suggests a classification confidence >80% (**Supplementary Note 1** and **Supplementary Fig. 7**); the residual cross-talk was 6% for both Atto 532 and Atto 565 (**Supplementary Fig. 8**). Because the *z* position is extracted from intensity ratios of channels with equal polarization (which are not influenced by the polarization properties of the filter), *z* localization can be performed as before (**Fig. 4d**). Localization precision was estimated to be σ_z = ~6 nm and σ_{xy} = ~12 nm for both dyes. By using the long-pass filter, we attenuated the total Atto 532 signal by 29% and the Atto 565 signal by 13%, which resulted in a relative reduction of the localization precision by 16% and 7%, respectively.

DISCUSSION

Given that the imaging is sufficiently fast, application of our 4Pi-SMS approach to dynamic studies in living cells should be feasible. In fact, a 4Pi setup using the same sample format was capable of

imaging living cells over many hours[27]. As for any method using opposing lenses, the maximum sample thickness is limited by refractive index in-homogeneities and the working distance of the lenses[28]. We derived the emitter localization under the assumption that the molecules can freely rotate. The asymmetric emission patterns arising from fixed or slowly rotating fluorophores compromise the localization; this caution applies to any stochastic method[22]. The much faster tumbling of molecules in aqueous media should help reduce the risk of mislocalizations. In any case, because of the fundamental nature of the increase of the total aperture of the system, which is conceptually orthogonal to the other concepts of resolution improvement, a 4Pi-SMS setup provides a 3D localization that is inherently superior to that of a related single-lens system.

The probability of incorrectly assigning a marker along the z axis depends on the number of detected photons, meaning that our method does not rule out z-position mislocalizations completely. However, for the fluorophores used here, this probability is negligible. Brighter labels will suppress these small artifacts even more while also increasing the simultaneously observable axial range. Extending the axial field of view should also be possible by incorporating optical elements for focal extension[29] into the detection path, concomitantly also raising the number of useful central moments. This measure can be useful if the axial range is so large that the combination of two central moments does not allow the extraction of a unique z position. Nonetheless, because markers outside the usable axial range can be discriminated, the simplest way to acquire large stacks is to scan the object along the z-axis, recording micron thick optical slices. Here we opted for the oscillations of the zeroth and third central moment for the z-position determination because it gave the best balance between precision and reliability. As we did not systematically search for the optimum estimator, it may be possible to improve our method by selecting other combinations of central moments, aperture weight functions or even other types of estimators while still exploiting the power of coherently synthesized 4Pi spherical wavefronts.

We used a single camera for all four detection channels. Although this reduces the field of view, it has advantages beyond saving money. The use of one rather than three (iPALM) or even four cameras[21] makes gain and quantum efficiency calibrations as well as synchronization obsolete.

In any setup that detects photons coherently through high aperture lenses, the fluorescence wavefronts are spherical. Therefore, our method should be directly applicable to the iPALM scheme. The localization precision in the z dimention just depends on the steepness of the oscillating intensities at a given z position and the photon budget, irrespective of the number of channels used. Four channels, however, allow the use of standard beam splitters and, more importantly, readily enable simultaneous multilabel recording by classification. The two-color image we obtained is just representative for a wide range of potential 4Pi-SMS microscopy applications in which three or even more fluorophore species are separated by color or by any other feature[26,30,31] such as anisotropy, rotational mobility[32] or lifetime, always providing the currently highest 3D localization precision achievable in a stochastic far-field optical nanoscopy scheme for the dyes in use.

METHODS

Methods and any associated references are available in the online version of the paper at http://www.nature.com/naturemethods/.

Note: Supplementary information is available on the Nature Methods website.

ACKNOWLEDGMENTS

We thank R. Pick for aid in the design of optics and mechanics, T. Gilat and E. Rothermel for technical assistance, and J. Keller for helpful discussions. We acknowledge J. Jethwa for critical reading of the manuscript. V. Belov (Max Planck Institute for Biophysical Chemistry, Göttingen) provided us with Rhodamine S and S. Takeoka (Waseda University, Tokyo) provided support on the nanosheets. This work was supported by the Gottfried Wilhelm Leibniz Program of the Deutsche Forschungsgemeinschaft (to S.W.H.) and a grant of the Deutsche Forschungsgemeinschaft to A.E. and S.W.H. (SFB 755).

AUTHOR CONTRIBUTIONS

A.E., A.S., T.L. and S.W.H. conceived and designed the study. D.A., C.G., C.A.W. and Y.O. performed experiments. D.A., A.E., A.S., C.v.M. and C.G. analyzed data. A.E., A.S., T.L. and S.W.H. wrote the manuscript.

COMPETING FINANCIAL INTERESTS

The authors declare no competing financial interests.

Published online at http://www.nature.com/naturemethods/.
Reprints and permissions information is available online at http://npg.nature.com/reprintsandpermissions/.

1. Hell, S. & Stelzer, E.H.K. Properties of a 4pi confocal fluorescence microscope. *J. Opt. Soc. Am. A Opt. Image Sci. Vis.* **9**, 2159–2166 (1992).
2. Gustafsson, M.G.L., Agard, D.A. & Sedat, J.W. I^{5}M: 3d widefield light microscopy with better than 100 nm axial resolution. *J. Microsc.* **195**, 10–16 (1999).
3. Egner, A., Jakobs, S. & Hell, S.W. Fast 100-nm resolution three-dimensional microscope reveals structural plasticity of mitochondria in live yeast. *Proc. Natl. Acad. Sci. USA* **99**, 3370–3375 (2002).
4. Egner, A. & Hell, S.W. Fluorescence microscopy with super-resolved optical sections. *Trends Cell Biol.* **15**, 207–215 (2005).
5. Schmidt, M., Nagorni, M. & Hell, S.W. Subresolution axial distance measurements in far-field fluorescence microscopy with precision of 1 nanometer. *Rev. Sci. Instrum.* **71**, 2742–2745 (2000).
6. Albrecht, B., Failla, A.V., Schweitzer, A. & Cremer, C. Spatially modulated illumination microscopy allows axial distance resolution in the nanometer range. *Appl. Opt.* **41**, 80–87 (2002).
7. Hell, S.W. Improvement of lateral resolution in far-field light microscopy using two-photon excitation with offset beams. *Opt. Commun.* **106**, 19–24 (1994).
8. Hell, S.W. & Wichmann, J. Breaking the diffraction resolution limit by stimulated-emission: stimulated-emission-depletion fluorescence microscopy. *Opt. Lett.* **19**, 780–782 (1994).
9. Hell, S.W. Far-field optical nanoscopy. *Science* **316**, 1153–1158 (2007).
10. Betzig, E. *et al.* Imaging intracellular fluorescent proteins at nanometer resolution. *Science* **313**, 1642–1645 (2006).
11. Rust, M.J., Bates, M. & Zhuang, X.W. Sub-diffraction-limit imaging by stochastic optical reconstruction microscopy (STORM). *Nat. Methods* **3**, 793–795 (2006).
12. Hess, S.T., Girirajan, T.P.K. & Mason, M.D. Ultra-high resolution imaging by fluorescence photoactivation localization microscopy. *Biophys. J.* **91**, 4258–4272 (2006).
13. Egner, A. *et al.* Fluorescence nanoscopy in whole cells by asnychronous localization of photoswitching emitters. *Biophys. J.* **93**, 3285–3290 (2007).
14. Bates, M., Huang, B., Dempsey, G.T. & Zhuang, X.W. Multicolor super-resolution imaging with photo-switchable fluorescent probes. *Science* **317**, 1749–1753 (2007).
15. Bock, H. *et al.* Two-color far-field fluorescence nanoscopy based on photoswitchable emitters. *Appl. Phys. B* **88**, 161–165 (2007).
16. Fölling, J. *et al.* Fluorescence nanoscopy by ground-state depletion and single-molecule return. *Nat. Methods* **5**, 943–945 (2008).
17. Heilemann, M., van de Linde, S., Mukherjee, A. & Sauer, M. Super-resolution imaging with small organic fluorophores. *Angew. Chem. Int. Ed.* **48**, 6903–6908 (2009).
18. Von Middendorff, C., Egner, A., Geisler, C., Hell, S. & Schonle, A. Isotropic 3D nanoscopy based on single emitter switching. *Opt. Express* **16**, 20774–20788 (2008).
19. Hell, S.W., Schmidt, R. & Egner, A. Diffraction-unlimited three-dimensional optical nanoscopy with opposing lenses. *Nat. Photonics* **3**, 381–387 (2009).

20. Schmidt, R. *et al.* Spherical nanosized focal spot unravels the interior of cells. *Nat. Methods* **5**, 539–544 (2008).
21. Shtengel, G. *et al.* Interferometric fluorescent super-resolution microscopy resolves 3D cellular ultrastructure. *Proc. Natl. Acad. Sci. USA* **106**, 3125–3130 (2009).
22. Engelhardt, J. *et al.* Molecular orientation affects localization accuracy in superresolution far-field fluorescence microscopy. *Nano Lett.* **11**, 209–213 (2011).
23. Okamura, Y. *et al.* Few immobilized thrombins are sufficient for platelet spreading. *Biophys. J.* (in the press).
24. Isenberg, W.M., McEver, R.P., Phillips, D.R., Shuman, M.A. & Bainton, D.F. The platelet fibrinogen receptor: an immunogold-surface replica study of agonist-induced ligand binding and receptor clustering. *J. Cell Biol.* **104**, 1655–1663 (1987).
25. Smith, C.M. II, Burris, S., Rao, G. & White, J. Detergent-resistant cytoskeleton of the surface-activated platelet differs from the suspension-activated platelet cytoskeleton. *Blood* **80**, 2774–2780 (1992).
26. Bossi, M. *et al.* Multi-color far-field fluorescence nanoscopy through isolated detection of distinct molecular species. *Nano Lett.* **8**, 2463–2468 (2008).
27. Egner, A., Verrier, S., Goroshkov, A., Soling, H.D. & Hell, S.W. 4Pi-microscopy of the Golgi apparatus in live mammalian cells. *J. Struct. Biol.* **147**, 70–76 (2004).
28. Egner, A., Schrader, M. & Hell, S.W. Refractive index mismatch induced intensity and phase variations in fluorescence confocal, multiphoton and 4pi-microscopy. *Opt. Commun.* **153**, 211–217 (1998).
29. Dowski, J., Edward, R. & Cathey, W.T. Extended depth of field through wave-front coding. *Appl. Opt.* **34**, 1859–1866 (1995).
30. Testa, I. *et al.* Multicolor fluorescence nanoscopy in fixed and living cells by exciting conventional fluorophores with a single wavelength. *Biophys. J.* **99**, 2686–2694 (2010).
31. Schoenle, A. & Hell, S.W. Fluorescence nanoscopy goes multicolor. *Nat. Biotechnol.* **25**, 1234–1235 (2007).
32. Testa, I. *et al.* Nanoscale separation of molecular species based on their rotational mobility. *Opt. Express* **16**, 21093–21104 (2008).

ONLINE METHODS

Setup design. The microscope design is illustrated in **Figure 1**, and the parts are listed in **Supplementary Note 2**.

Setup characterization. To characterize the setup, we used fluorescent beads (FluoSpheres carboxylate-modified microspheres, 100 nm specified diameter, red fluorescent 580/605; Invitrogen), diluted 1:5,000 in distilled water. We placed the solution on a coverslip treated with poly(L-lysine) (Sigma-Aldrich) solution, 0.1% (w/v) in H_2O. The solution was incubated for 10 min. To remove unattached beads, the sample was rinsed with water. After adding 10 µl distilled water as medium, the sample was covered by a second coverslip and sealed with nail polish. We recorded a gauge measurement by scanning a bead over a range of 2 µm in 40 nm steps with a camera exposure time of 100 ms. A 532 nm solid-state laser (DPSS 532, HB-Laserkomponenten) was used as the excitation source. To characterize the setup, we scanned the bead over the central 1 µm range in 40-nm steps and recorded 300 images per *z* step. Here the exposure time was 10 ms at an excitation intensity of ~1 kW cm^{-2}. The localization precision was explored as a function of the emitter brightness (**Supplementary Fig. 5**). Estimates for the localization precision in our experiments were thus obtained by scaling the results from our gauge measurements according to the actual marker brightness. Calculation of the confidence level and cross-talk estimation in two-color experiments was performed as before[26] (**Supplementary Note 1**).

Samples for platelet imaging. Platelets were obtained from blood withdrawn from healthy individuals. Written informed consent was obtained according to the guidelines of the institutional review board of the University of Bonn. To the platelets a 10% volume of 3.8% (w/v) sodium citrate in water was added. Platelet-rich plasma was obtained from the supernatant after a centrifugation step (120*g*, 15 min, 22 °C) and a 15% volume of a acid citrate–dextrose solution (2.2% (w/v) sodium citrate, 0.8% (w/v) citric acid, 2.2% (w/v) glucose and 2 µM prostaglandin E1 (PGE_1; Sigma-Aldrich)) was added. The suspension was centrifuged (1,500*g*, 7 min, 22 °C) yielding a platelet pellet, which was resuspended in Ringer's citrate dextrose solution (0.76% (w/v) citric acid, 0.09% (w/v) glucose, 0.043% (w/v) $MgCl_2$, 0.038% (w/v) KCl, 0.6% (w/v) NaCl and 2 µM PGE_1; pH 6.5)). The suspension was centrifuged (1,520*g*, 7 min, 22 °C) and the pellet was resuspended in HEPES-tyrode buffer (5.6 mM glucose, 10 mM HEPES, 2.7 mM KCl, 1 mM $MgCl_2$, 137 mM NaCl, 12 mM $NaHCO_3$ and 0.4 mM NaH_2PO_4; pH 7.4) containing 1 mM $CaCl_2$ to yield a platelet concentration of 2.0×10^5 $µl^{-1}$.

Platelets in HEPES-tyrode buffer were placed onto coverslips carrying a thrombin-coated nanosheet[23,33] (coating was performed with 10 U ml^{-1} thrombin overnight at 4 °C) and incubated for 10 min at 37 °C. After incubation, the non-adherent platelets were washed off. Then cells were fixed for 90 min with 4% (w/v) paraformaldehyde (PFA) in PBS at 4 °C, quenched in PBS containing 50 mM NH_4Cl at room temperature (~21–25 °C) for 10 min and washed in PBS three times for 5 min each. Then the platelets were extracted using 0.5% (v/v) Triton X-100 in PBS for 10 min at room temperature and incubated at room temperature for 45 min with monoclonal mouse antibody to human GPIIb (BD Biosciences) in 3% (w/v) BSA in PBS containing 0.2% (v/v) Triton X-100. Subsequently they were washed in PBS three times for 10 min, followed by a 45-min incubation with secondary antibody using either custom-labeled Rhodamine S or Atto 532 sheep anti-mouse (ATTO-TEC) in 3% (w/v) BSA in PBS containing 0.2% (v/v) Triton X-100. Finally, they were washed in PBS three times for 10 min each and shipped in 4% PFA in PBS to the Max Planck Institute for Biophysical Chemistry.

Upon arrival, PFA was quenched for 10 min at room temperature with a PBS solution containing 50 mM NH_4Cl. For imaging, samples were mounted in Tris buffer (50 mM Tris-HCl and 10 mM NaCl; pH 7.4) containing 10% (w/v) glucose, 0.25 mg ml^{-1} glucose oxidase, 0.06 mg ml^{-1} catalase and 100 µM Trolox (Sigma-Aldrich). They were covered with a second coverslip that was sparsely coated with fluorescent beads (FluoSpheres, carboxylate-modified microspheres, 100 nm specified diameter, orange fluorescent 540/560; Invitrogen) as described above to facilitate the initial alignment of the microscope and for gauge measurements. We acquired 30,000 (Rhodamine S) and 120,000 (Atto 532) images at 100 Hz, exciting with a 532 nm laser at an intensity of 7–14 kW cm^2 and registered on average 800 (Rhodamine S) and 380 (Atto 532) photons per event. Rhodamine S switches irreversibly from the off to the on state, therefore each Rhodamine S molecule generates at most one detected event. Atto 532 switches reversibly between the on and the off state; therefore, each Atto 532 molecule might generate multiple detected events.

Samples for imaging of the tubulin cytoskeleton. For immunolabeling tubulin, cultured Vero cells, originating from the African green monkey (kidney epithelia), *Chlorocebus* sp., were grown on coverslips overnight. For immunological labeling, the cells were fixed for 5 min with ice-cold methanol (absolute). After washing in PBS (137 mM NaCl, 3 mM KCl, 8 mM Na_2HPO_4 and 1.5 mM KH_2PO_4; pH 7), the samples were blocked with 5% (w/v) BSA in PBS and incubated with mouse monoclonal antibodies to α-tubulin (Sigma Aldrich). The primary antibodies were detected with secondary antibodies (sheep anti-mouse; Jackson ImmunoResearch Laboratories) custom-labeled with Rhodamine S.

The samples were spin-coated with 4% (w/v) polyvinyl alcohol (PVA), mounted in PBS (pH 7.0) and covered with a second coverslip that was sparsely coated with fluorescent beads (FluoSpheres carboxylate-modified microspheres, 100 nm specified diameter, orange fluorescent 540/560; Invitrogen) as described above. We acquired 110,000 images at 100 Hz, exciting with a 532-nm laser at an intensity of 7–14 kW cm^{-2}, and registered on average 700 photons per event. As Rhodamine S switches irreversibly from the off to the on state, each dye molecule generates at most one detected event.

Samples for two-color imaging. For immunolabeling of tubulin and PMP70, cultured PtK2 cells, originating from the marsupial (kidney epithelia), *Potorous tridactylus*, were grown on coverslips overnight. For immunological labeling, the cells were fixed for 5 min with ice-cold methanol (absolute). After washing in PBS, the samples were blocked with 5% (w/v) BSA in PBS and incubated with mouse monoclonal antibodies to α-tubulin (Sigma Aldrich) and polyclonal rabbit antibodies to PMP70 (Abcam). The primary antibodies were detected with secondary antibodies (sheep anti-mouse and goat anti-rabbit; Jackson ImmunoResearch Laboratories) custom-labeled with Atto 565 and Atto 532 (ATTO-TEC).

doi:10.1038/nmeth.1583

To create an oxygen-free environment for imaging, the samples were mounted in Tris buffer containing glucose oxidase and catalase (Sigma Aldrich), as described above.

Finally, all samples were covered with a second coverslip that was sparsely coated with fluorescent beads (FluoSpheres carboxylate-modified microspheres, 100 nm specified diameter, orange fluorescent 540/560 and red fluorescent 580/605; Invitrogen) as described above. We acquired 30,000 images at 100 Hz by exciting with a 532-nm laser at an intensity of 7–14 kW cm^{-2}, and registered on average 520 photons (Atto 532) and 500 photons (Atto 565) per event. As Atto 532 and Atto 565 switch reversibly between the on and the off state, each dye molecule might generate multiple detected events.

33. Okamura, Y., Kabata, K., Kinoshita, M., Saitoh, D. & Takeoka, S. Free-standing biodegradable poly(lactic acid) nanosheet for sealing operations in surgery. *Adv. Mater.* **21**, 4388–4392 (2009).